

REPORT DOCUMENTATION PAGE					Form Approved OMB No. 0704-0188	
The public reporting burden for this collection of information is estimated to average 1 hour per response, including the time for reviewing instructions, searching existing data sources, gathering and maintaining the data needed, and completing and reviewing the collection of information. Send comments regarding this burden estimate or any other aspect of this collection of information, including suggestions for reducing the burden, to Department of Defense, Washington Headquarters Services, Directorate for Information Operations and Reports (0704-0188), 1215 Jefferson Davis Highway, Suite 1204, Arlington, VA 22202-4302. Respondents should be aware that notwithstanding any other provision of law, no person shall be subject to any penalty for failing to comply with a collection of information if it does not display a currently valid OMB control number.						
PLEASE DO NOT RETURN YOUR FORM TO THE ABOVE ADDRESS.						
1. REPORT DATE (DD-MM-YYYY) 23-12-2011		2. REPORT TYPE Final		3. DATES COVERED (From - To) 1 June 2009 - 30 November 2011		
4. TITLE AND SUBTITLE DCT-TCI: Real Gas Characterization of Plasma Flow Control-An Integrated Approach				5a. CONTRACT NUMBER		
				5b. GRANT NUMBER FA9550-09-1-0372		
				5c. PROGRAM ELEMENT NUMBER		
				5d. PROJECT NUMBER		
6. AUTHOR(S) Subrata Roy, Chin-Cheng Wang and Ryan Durscher				5e. TASK NUMBER		
				5f. WORK UNIT NUMBER		
7. PERFORMING ORGANIZATION NAME(S) AND ADDRESS(ES) University of Florida Mechanical and Aerospace Engineering 231 Aerospace Building Gainesville FL 32611-6250				8. PERFORMING ORGANIZATION REPORT NUMBER		
9. SPONSORING/MONITORING AGENCY NAME(S) AND ADDRESS(ES) AF Office of Scientific Research 875 N. Randolph St. Room 3112 Arlington, VA 22203				10. SPONSOR/MONITOR'S ACRONYM(S) AFOSR/RSA		
				11. SPONSOR/MONITOR'S REPORT NUMBER(S) AFRL-OSR-VA-TR-2012-0541		
12. DISTRIBUTION/AVAILABILITY STATEMENT Approved for Public Release; distribution is unlimited.						
13. SUPPLEMENTARY NOTES						
14. ABSTRACT This report presents results culminated partially from the AFOSR grant FA9550-09-1-0372 on experimental and numerical characterization of novel plasma actuators. Specifically the serpentine and multi-barrier plasma actuators are considered. The serpentine geometry demonstrated capability for the inducement of fully three dimensional vortical structures. The nature of the fluid flow inducement on a flat plate, in quiescent conditions, due to dielectric barrier discharge (DBD) plasma actuators is numerically and experimentally investigated. The three-dimensional plasma kinetic equations are solved using our in-house multi-scale ionized gas (MIG) flow code. Numerical results show detailed distribution of electron temperature and three dimensional plasma force vectors. Three-dimensional effects such as pinching and spreading the neighboring fluid are observed. The mechanisms of vorticity generation for DBD actuators are discussed. Also, the influence of applied voltage is studied. To quantify these effects stereo particle image velocimetry (PIV) is used to generate time averaged						
15. SUBJECT TERMS Plasma Actuators, Serpentine Geometry, Multi-Barrier Plasma Actuators, Stereo PIV Experiment, MIG Plasma Kinetic Simulation						
16. SECURITY CLASSIFICATION OF:			17. LIMITATION OF ABSTRACT	18. NUMBER OF PAGES	19a. NAME OF RESPONSIBLE PERSON	
a. REPORT	b. ABSTRACT	c. THIS PAGE			Dr. S Roy	
U	U	U	U	18	19b. TELEPHONE NUMBER (Include area code) 352-392-9823	

Reset

DCT-TCI: REAL GAS CHARACTERIZATION OF PLASMA FLOW CONTROL-AN INTEGRATED APPROACH

Subrata Roy^a, Chin-Cheng Wang and Ryan Durscher
*Computational Plasma Dynamics Laboratory and Test Facility,
Applied Physics Research Group, Department of Mechanical and Aerospace Engineering,
University of Florida, Gainesville, FL 32611, USA*

ABSTRACT

This report presents results culminated partially from the AFOSR grant FA9550-09-1-0372 on experimental and numerical characterization of novel plasma actuators. Specifically the serpentine and multi-barrier plasma actuators are considered. The serpentine geometry demonstrated capability for the inducement of fully three-dimensional vortical structures. The nature of the fluid flow inducement on a flat plate, in quiescent conditions, due to dielectric barrier discharge (DBD) plasma actuators is numerically and experimentally investigated. The three-dimensional plasma kinetic equations are solved using our in-house multi-scale ionized gas (MIG) flow code. Numerical results show detailed distribution of electron temperature and three dimensional plasma force vectors. Three-dimensional effects such as pinching and spreading the neighboring fluid are observed. The mechanisms of vorticity generation for DBD actuators are discussed. Also, the influence of applied voltage is studied. To quantify these effects stereo particle image velocimetry (PIV) is used to generate time averaged, spatially resolved measurements of the detailed flow structure. The multi-barrier plasma actuator (MBPA) is introduced to improve the effectiveness of plasma actuators. The MBPA design incorporates multiple dielectric layers and phase lagged powered electrodes into the standard design. The results of MBPA show higher induced velocities/resultant forces. For all test cases the total power delivered to the actuator is calculated and presented. These designs could be beneficial for rapid mixing of the local fluid. Experimental data for serpentine and multi-barrier plasma actuators are reported for validation purpose.

I. INTRODUCTION

The plasma actuator is becoming a popular device for active flow control. A few advantages of the plasma actuators are surface compliance, rapid response, lack of moving parts, and easy installation. Specifically, due to the lack of mechanical components the life time of the actuator could be significantly extended as compared to other mechanical/electromechanical devices such as synthetic jet actuators. Reported experimental and numerical results¹⁻² show that dielectric barrier discharge (DBD) actuators are effective in controlling the flow at low freestream velocities ($\sim 20\text{m/s}$). One major impediment affecting the working speed is the inducement of a thin boundary layer which is limited by wall shear. So it is important to design actuators which can inject momentum into the boundary layer resulting in a much thicker layer shown in FIG. 1.³ Figure 1 shows a serpentine design that ensures a fully three-dimensional flow control mechanism using a single actuator combining the effects of a standard linear actuator and a plasma synthetic jet actuator (PSJA)⁴. Intuitively as one moves along the span of the actuator there is a spreading of the fluid at the crest while there is a pinching in the trough. Such a disturbance will result in an enhanced mixing of the surrounding fluid. This was first numerically proposed by Roy and Wang³ who applied the actuator to modify flow over a flat plate. The serpentine configuration has also been explored numerically for the control of flows over a flapping⁵ and

^{a)} Electronic mail: roy@ufl.edu

stationary⁶ airfoil representative of micro air vehicle (MAV) applications. In this paper, we will study both numerical simulation and experimental work for the serpentine actuator.

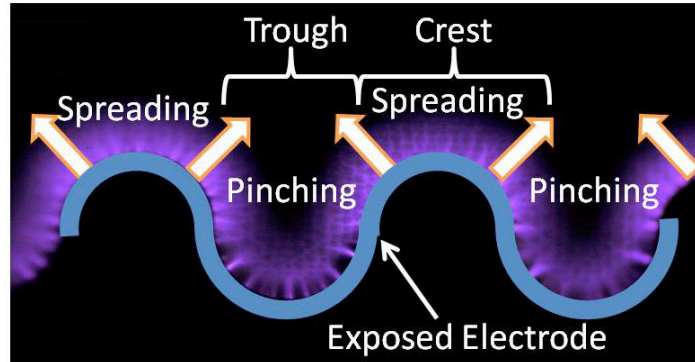


FIG. 1. A serpentine DBD plasma actuator.

Many researchers⁷⁻⁸ have demonstrated aerodynamic applications of standard DBD actuators on a flat plate at atmospheric pressure. These actuators produced reasonable thrust by asymmetric spanwise electrode configurations. Numerical models of plasma actuators also range from simplified estimation of the force field with an assumed plasma distribution to detailed air chemistry based plasma kinetic simulation.⁹⁻¹² Other researchers have developed reduced order force models¹¹ based on semi-empirical⁹⁻¹⁰ or physics based formulation¹². They considered not only the geometry effects but also plasma parameters. The fidelity of these methods is better than phenomenological model but is yet to explain the operational physics of DBD actuators. Some reduced order models may work well for standard linear actuators but not for serpentine actuators due to lack of physics understanding of such actuators. First-principles analysis is a high-fidelity model to examine the physics of plasma actuators. While it is feasible to incorporate a large number of species into the air chemistry model, it becomes computationally impractical to solve them for a kHz frequency dielectric barrier discharge actuator problem. A reasonable way is to solve coupled system of plasma governing equations and Poisson's equation which is the so-called physics based first-principles analysis. Roy *et al.*¹³⁻¹⁵ presented a well-established model to describe detailed densities of electrons, positive and negative charged and neutral species with Poisson's equation to obtain temporal and spatial profiles of voltage and densities. They demonstrated the model predictions for charge densities, electric field, and gas velocity distributions, and showed trends that mimic reported experimental data.

In our prior study³, we presented the interaction of a serpentine actuator with a co-flow or counter-flow on a flat surface. The results showed three-dimensional plasma effects extract momentum from an upstream flow injecting it into the bulk fluid through localized pinching and spreading effects. Such three-dimensional actuators produced better flow mixing downstream of the actuator than the standard two-dimensional (linear) DBD actuators. The results of the simulation also show similar vortex generating capabilities to that of the actuator configuration used by Schatzman and Thomas¹⁶. However, instead of using an array of actuators, only a single actuator is needed in the serpentine design. This could potentially lead to lower power consumption and less electrical circuitry.

Varying aspects of this conventional design such as electrode geometry, input voltage, dielectric material, electrode spacing, voltage waveform, and driving frequency have been investigated by numerous authors. A recent annual review² provides a brief overview of these efforts and current attempts to combine them into an optimized device. Although these efforts have provided improved operation as well as a great deal of insight into the operational mechanisms of the DBD plasma actuator, there is still a need for higher performance. In an

attempt to meet this need the concept of multi-barrier plasma actuators (MBPA) was presented in a patent by Roy.¹⁷ The MBPA is an extension on the single layer asymmetric geometry described above to include additional dielectric layers and powered electrodes kept at phase differences (FIG. 2). Such a configuration opens up additional parameters to the DBD actuator design space. Preliminary results on these multi layer configurations previously indicated¹⁸ that the multi-barrier designs were capable of achieving higher resultant thrusts than what was considered the standard actuator configuration. The effectiveness which is a ratio of measured thrust to consumed power was also found to improve.

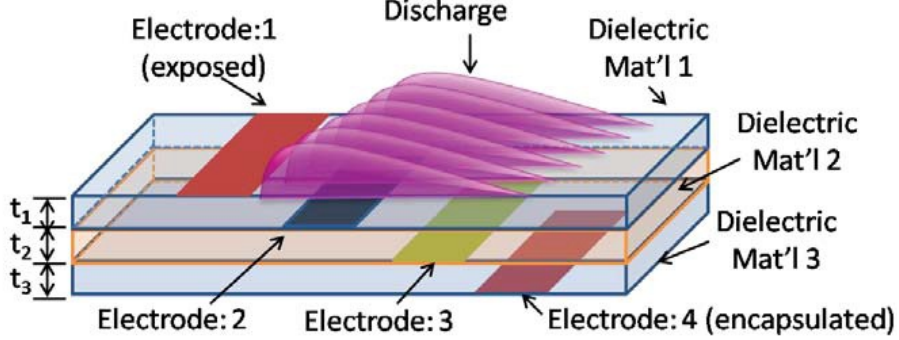


FIG. 2. Tri-layer multi-barrier plasma actuator (MBPA) schematic.

In the present study we characterize the induced flow field generated by serpentine in quiescent air. For high-fidelity force distribution of serpentine design, we employ physics based first-principles analysis to resolve the plasma force vectors distribution over a flat surface. Furthermore, we identify the effects of the geometric wavelength and amplitude of the serpentine. The nonintrusive flow diagnostic technique of particle image velocimetry (PIV) is used to quantify the effects of these actuators. A stereo-PIV system is used to capture time averaged, spatially resolved data sets of the vector fields along spanwise and streamwise cuts. The two-dimensional planes are then reconstructed to give a three-dimensional view of the induced flow field structure. For the MBPA design, the resultant thrust from both bi-layer and tri-layer designs are measured and compared with the standard actuator. The influence of mixing two different dielectric materials into a single actuator is also addressed. For each configuration the total consumed power and the effectiveness is calculated and compared against the standard design. The detailed numerical model is summarized in the section II. Section III describes the cases of numerical simulation and experimental setup for plasma actuators. Section IV presents the results of serpentine and multi-barrier configurations. Finally, conclusions and future works are drawn in section V.

II. MODEL DETAILS

The three-dimensional drift-diffusion plasma governing equations as well as Navier-Stokes equations are solved in this study. We utilize the two-species basic model to reduce the computational complexity of plasma chemistry in three-dimensions. The unsteady transport for ions and electrons is derived from the first-principles in the form of conservation of species continuity. The three-dimensional equations for determining concentrations of positive ion n_i and electron n_e together with Poisson equation for electric field vector \mathbf{E} (E_x, E_y, E_z) are described in prior publication¹⁹. The discharge is maintained using a Townsend ionization scheme. The charged species β (e, i) is given by the drift-diffusion approximation as $n_\beta \mathbf{V}_\beta = \text{sgn}(e) n_\beta \mu_\beta \mathbf{E} - D_\beta \nabla n_\beta$. Finally, we end up with the following equations:

$$\begin{aligned} \frac{\partial n_\beta}{\partial t} + \frac{\partial}{\partial x} \left\{ \text{sgn}(e)n_\beta \mu_\beta E_x - D_\beta \frac{\partial n_\beta}{\partial x} \right\} + \frac{\partial}{\partial y} \left\{ \text{sgn}(e)n_\beta \mu_\beta E_y - D_\beta \frac{\partial n_\beta}{\partial y} \right\} \\ + \frac{\partial}{\partial z} \left\{ \text{sgn}(e)n_\beta \mu_\beta E_z - D_\beta \frac{\partial n_\beta}{\partial z} \right\} = \alpha |\Gamma_e| - r n_i n_e \end{aligned} \quad (1)$$

where $\mu_i = 1.45 \times 10^3 / p$ (cm²/sV) is the ion mobility, $\mu_e = 4.4 \times 10^5 / p$ (cm²/sV) is the electron mobility, D_i and D_e are the ion and electron diffusion coefficients calculated from the Einstein relation which is a function of ion and electron mobility as well as ion and electron temperature, i.e. $D_i = \mu_i T_i$ and $D_e = \mu_e T_e$.

We assume that the electrons are in local thermal equilibrium (LTE), and the mean energy of streamer head equilibrate in the presence of the electric field as a function of local (E/N). The electron temperature T_e in the plasma is proportional to the ratio of the electric field to the density of neutral particles (E/N). The electron temperature in electron volts can be determined according to the expression, $T_e = (E/N)/(2\sigma\sqrt{2m_e/m_i})$, where σ is the cross-section of electron–neutral collisions.²⁰ We consider isothermal ions and neutrals.

A domain of (-39.6:39.6×-21.6:21.6×0.0:24.0) mm is considered for the plasma simulation. A 2.4 mm thick Teflon dielectric is used with relative dielectric constant of 2. The mesh size is 89×49×41 nodes. The numerical model for solving DBD plasma governing equations uses an efficient finite element algorithm for solving partial differential equations (PDE) approximately. The solution methodology anchored in the in-house modular MIG flow code is based on the Galerkin Weak Statement (GWS) of the PDE which is derived from variational principles. An iterative sparse matrix solver, Generalized Minimal RESidual (GMRES), is utilized to solve the resultant stiff matrix. The fully implicit time stepping procedure along with the Newton-Raphson scheme is used for dealing with this nonlinear problem. The solution is assumed to have converged when the L_2 norms of all the normalized solution variables and residuals are below a convergence criterion of 10^{-3} .

The time-average of the spatial distribution of electric force density, $\mathbf{F} (: F_x, F_y, F_z) = eq\mathbf{E}$, is introduced into the commercial Navier-Stokes solver, ANSYS Fluent, as a source term in the momentum equations using user defined functions (UDF). A second-order upwind spatial discretization method is used to solve for the induced flow on a computational mesh of 500,000 fluid volumes. Convergence is determined when the residual among the continuity and momentum equations are less than 10^{-3} .

III. PROBLEM DESCRIPTIONS

A. Numerical Simulation

The plasma actuators are assumed to be flushed mounted at the center of a quiescent domain with dimensions (-0.1:0.1×-0.1:0.1×0.0:0.1) m. The right side of the domain ($y = 0.1$ m) is considered to be the inlet, while the top ($z = 0.1$ m) and left ($y = -0.1$ m) sides are outflow boundaries. The gauge pressure at the outlet boundaries is maintained at 0 Pa. Symmetry is considered on the domain's side walls ($x = \pm 0.1$ m), while no slip is enforced on the lower boundary ($z = 0.0$ m). The thickness of the dielectric material and electrodes are neglected in the flow simulations. Air is considered to be the working fluid.

The three-dimensional effects of serpentine plasma actuators are studied. Upon applying a sufficient electric field to the exposed electrode to induce an electrical breakdown, an electro-hydrodynamic (EHD) body force is generated along the electrode (FIG. 1). This electric force interacts with bulk fluid and induces vortices locally and downstream of the actuator. Such effects induce a three-dimensional swirling flow in the vicinity of the plasma region. The mechanisms of vorticity generation using the serpentine actuator will be explained in the result section. For the cases of changing wavelengths, the wavelength is varied from 10 to 30 mm with the

amplitude fixed at 8 mm. On the other hand, the amplitude is increased from 4 to 16 mm for a fixed wavelength of 10 mm.

B. Actuator Construction and Designs

A photo-fabrication method is used to construct the continuously curved electrode shape of the serpentine actuator. Such a method is widely used in the electronics community for in-house printed circuit board (PCB) fabrication. Sheets of copper tape with a nominal thickness of 0.07 mm were first adhered to both sides of the acrylic dielectric substrate which has a relative dielectric constant of 3.0. Copper tape was first adhered to both sides of a 3 mm thick acrylic plate. A negative photo-resist, a transparent film and a UV light were then employed to imprint the specific serpentine design on the copper which was then selectively removed after being submerged in a bath of ferric chloride. The reminiscence of the adhesive glue left behind by the copper tape was removed using a solvent such as methanol or acetone. The width of the exposed and grounded electrode is 2 mm which are kept at a uniform horizontal gap of 2 mm. The serpentine actuator used is constructed from patterned circular arcs. The wavelength (λ) of this serpentine design is 20 mm and the amplitude (Λ) is 8 mm. To prevent end effects from influencing the velocity measurements, the tested actuators consisted of 4.5 periods for an overall crosswise length, l , of 90 mm.

General schematics of the two serpentine designs investigated in this work are shown in FIG. 3: one with patterned circular arcs (FIG. 3b), and one with patterned rectangles (FIG. 3c). For both designs tested, the width of the exposed electrode, w_1 , was fixed at 2 mm and there was no horizontal displacement between the electrodes. In the patterned circular arcs design (FIG. 3b) the radii of the inner edge of the exposed electrode are 6 (r_1) and 4 (r_2) mm. The lower, grounded electrode in this design has a width, w_2 , of 5 mm which follows along the inner radius of the exposed electrode. The dimensions for the patterned rectangular design are shown in FIG. 3c by $g_1 = 2r_1 = 12$ mm, $g_2 = r_1 + r_2 = 10$ mm, $g_3 = w_2 = 5$ mm, and $g_4 = 2r_2 = 8$ mm. The grounded electrode for this design again follows along the windings of the exposed electrode but for simplicity of fabrication the excess grounded electrode was not removed in the trough region. The wavelength (λ), or the length over which the pattern repeats itself, for both designs was 20 mm. To prevent end effects from influencing the velocity measurements, the actuators tested consisted of 8 and 9 wavelengths for the circular and rectangular designs, respectively. This corresponds to overall spanwise (z-direction) lengths, l_{span} , of 160 mm and 180 mm.

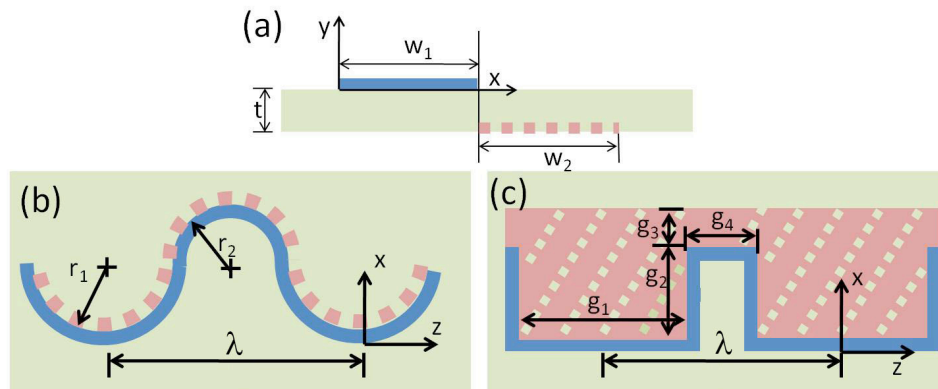


FIG. 3. Schematics of the side (a) and top (b-circular, c- rectangular) views of the serpentine actuators tested.

A general schematic of the electrode configurations used in this work are shown in FIG. 4. The standard DBD design, a bi-layer configuration, and trilayer layout are represented by a, b, and c respectively. One will note that the overall thickness, t , of the combined dielectric materials remains the same between the different cases. The overall thickness, t , of the actuators investigated, with the exception of the mixed dielectric cases, was 6 mm. Similarly the horizontal footprint also remains the same between the configurations at $3w$, where w corresponds to the exposed electrode's width, 5 mm. For all three designs the exposed (top) electrode is powered with a peak potential at some reference phase angle. As described previously the lower electrode for the standard actuator design is grounded. For the multi-barrier cases (FIG. 4b and FIG. 4c) the additional electrodes are also supplied with a potential but are now temporally shifted by some phase angle relative to the exposed electrode. A positive phase angle refers to a leading phase angle while negative values are considered lagging. The electrodes in the designs are constructed from adhesively backed copper tape with a thickness of 70 μm . In all configurations the electrodes had a length of 120.0 mm. The dielectric substrate used (again with the exception of the mixed dielectric cases) was acrylic. The layers of the multi-barrier actuators are held together using a two part epoxy. The epoxy layers were found to have thicknesses varying from 60-150 μm depending on the actuator. It is assumed, however, that the epoxy has a negligible influence on the plasma formation due to its relatively small thickness.

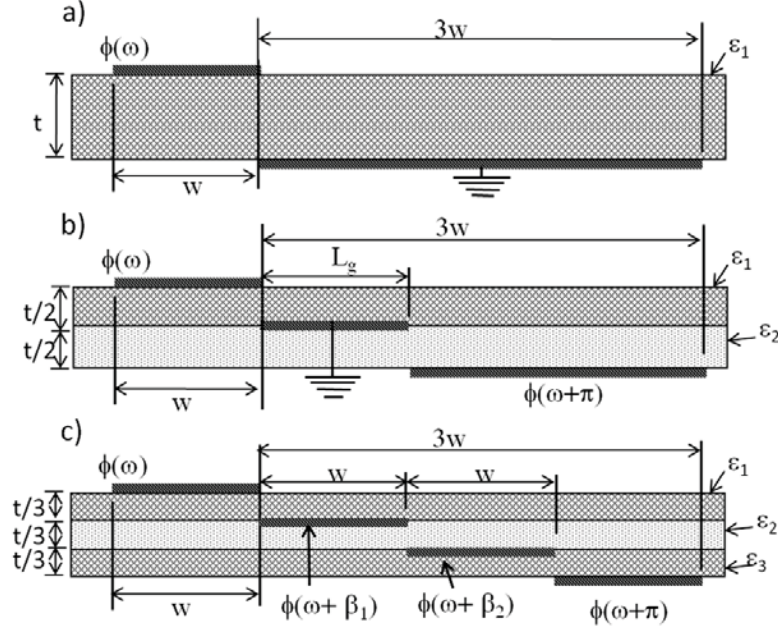


FIG. 4. Schematics of actuator designs tested: a) standard actuator design, b) bi-layer MBPA, and c) tri-layer MBPA.

C. Plasma Generation for the Serpentine Actuator

The high voltages required to ignite the plasma discharge were generated using a Corona Magnetics Inc. high voltage transformer. A 10 kHz sinusoidal waveform was produced using a Tektronix arbitrary waveform generator (AFG3022B) and was further amplified using a QSC audio amplifier (RMX 2450). The voltage and current delivered to the actuator were monitored using a Tektronix high-voltage probe (P6015A) along with a Pearson Electronics ammeter (2100). The outputs from the probes were sampled at 250 MSa s^{-1} using a digitizing oscilloscope (Tektronix DPO3014). A 20.0 MHz low-pass filter was implemented on the oscilloscope for the channel connected to the current probe. In a single acquisition the oscilloscope captured 10^6 points. As

such, 10 acquisitions were seized for each planar cut which corresponds to 400 periods over which the power delivered to the actuator is averaged.

D. Plasma Generation for the MBPA

The multi-barrier plasma actuator requires multiple high voltage, AC signals in which the relative phase angles between the signals can be precisely controlled/manipulated. For the single and bi-layer actuators such signals originated from a dual output function generator (Tektronix AFG 3022B), where an 8 channel analog output PCI card (NI PCI-6713) and a LabVIEW interface was used for the tri-layer configuration. The low voltage sinusoidal waveforms at a driving frequency of 14 kHz were further amplified by dual channel audio amplifiers (QSC RMX 2450). The high voltage required to achieve a breakdown of the surrounding air was finally reached using a Corona Magnetics, Inc. high-voltage transformer. An example circuit configuration used to drive a tri-layer MBPA is shown in FIG. 5.

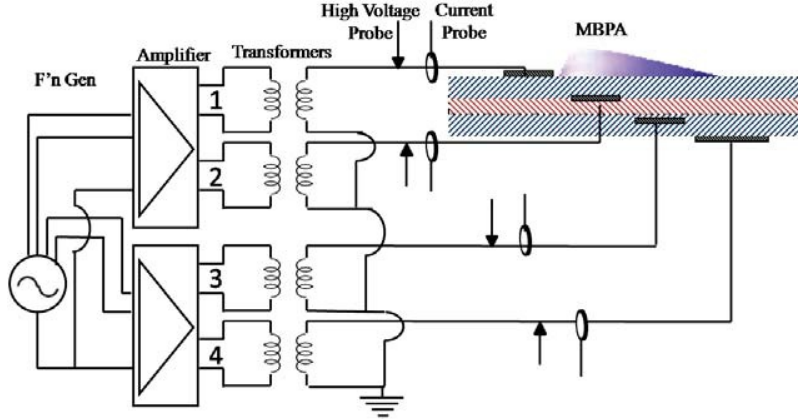


FIG. 5. Circuit schematic used to generate a DBD discharge for a tri-layer multi-barrier plasma actuator.

As shown in the above diagram the voltage and current flowing through each branch in the circuit was monitored using high voltage and current probes. The voltage probes used were Tektronix's P6015A while Pearson Electronic's 2100 and Bergoz's CT-F1.0-B measured the current. Note that the primary difference between the two different ammeters was their respective bandwidth limits which had corresponding upper limits of 20 MHz and 100 MHz. For simplicity a 20 MHz bandwidth limit was set on the digitizing oscilloscopes regardless of which current probe was used. The oscilloscopes used to capture the voltage and current waveforms were Tektronix's DPO3014 and DPO2014. In a single acquisition the oscilloscopes captured 1 million points for each waveform at a sampling rate of 250 MSa/s.

For each input voltage for the standard and bi-layer configurations, 10 acquisitions were recorded which corresponds to 560 periods over which the calculated power is averaged. Conversely, due to the large amount of data downloaded, only 2 acquisitions (112 periods) were recorded for the tri-layer actuators. The total power, P_{tot} , delivered to the plasma actuator was considered to be a linear combination of the measured power flowing through each branch of the circuit (referring to FIG. 5). For example, the standard actuator has 1 branch, the bi-layer has 2, and the tri-layer has 4. The power delivered in each branch of the circuit was calculated based on summing the product of the instantaneous voltage, V , and current, I , and then dividing by the total number of acquired points as follows.

$$P_{tot} = \frac{1}{N} \left(\sum_{i=1}^N V_{i,1} I_{i,1} + \sum_{i=1}^N V_{i,2} I_{i,2} + \sum_{i=1}^N V_{i,3} I_{i,3} + \sum_{i=1}^N V_{i,4} I_{i,4} \right) \quad (2)$$

E. Particle Image Velocimetry

The standard linear plasma actuator is generally considered to be a two-dimensional device, indicating that the body force vector only has two components (x , y). This assumption does not hold, however, for the serpentine design. By nature of its configuration, fluid is pushed in all three directions. To capture these effects we use a stereoscopic particle image velocimetry system to spatially resolve the three components of induced velocity vectors for a given two-dimensional plane.

The actuator is setup in a 61 x 61 x 120 cm quiescent chamber shown in FIG. 6a. The floor of the chamber is connected to a single axis manual traverse (Velmex A1503P40-S1.5), which allows the floor to translate horizontally ± 19 mm off center. This eliminated the need to continuously readjust the stereo optics. Two of LaVision's ImagerPro X 4M (2048 x 2048 pixels) cameras in combination with 105 mm macro lenses and 1.4x teleconverters were used to capture the PIV images. The cameras were aligned nearly perpendicular to the light sheet (FIG. 6) and had a relative angle of $\sim 58^\circ$ between them. The field of view for each image was approximately 45 x 45 mm. A light sheet cutting along the actuator was generated using a Nd:YAG dual cavity pulsed 532 nm laser (New Wave Research Solo PIV II 30). A TSI atomizer (Model 9302) along with Ondina oil was used to seed the chamber. The atomizer produces a droplet with a mean diameter of $\sim 0.8 \mu\text{m}$ when pressurized at 25 psi.²¹ Ondina is assumed to be dipole neutral and thus unaffected by the high electric field near the actuator.

LaVision's DaVis 7.2 3D-PIV software package was used to calibrate, capture, pre-process, and process the PIV images. Image calibration was initially done with a 40 mm x 40 mm, two tiered calibration plate and was later refined using LaVision's self-calibration wizard.²² A refining, multi-grid, stereo cross-correlation process was carried out on each image pair resulting in a final vector field resolution of 0.39 mm. To ensure statistical convergence of the velocity field, 200 image pairs were taken for each spanwise and streamwise cut. The vector fields were found to converge after ~ 150 acquisitions. Furthermore, for each planar slice two different time delays (between laser pulses), dt , were investigated. All results reported here are for a $dt = 50 \mu\text{s}$ as there were no discernible difference with that of a $30 \mu\text{s}$ delay. Regardless of the time separations investigated the resulting structure of the flow field remained essentially the same, with the average peak velocities varying no more than ~ 0.1 m/s for each case.

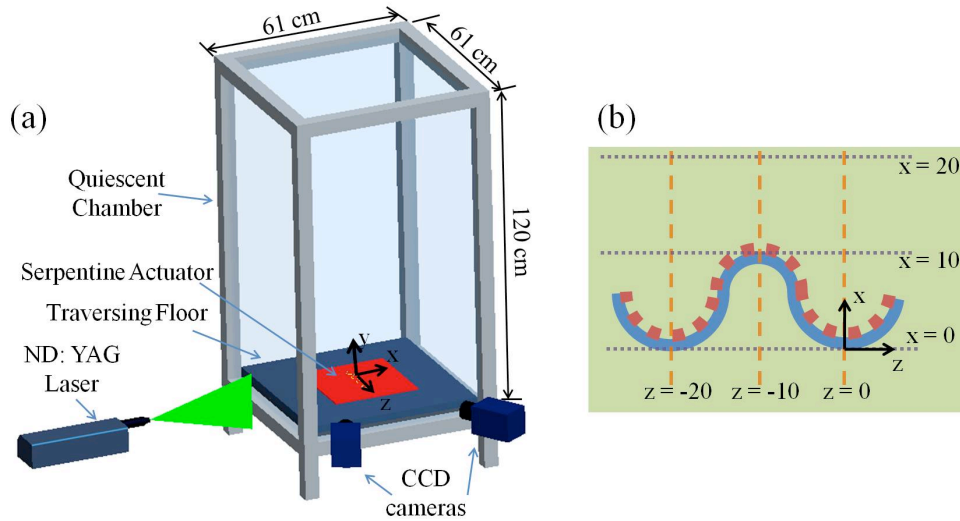


FIG. 6. (a) The stereo-PIV setup, and (b) locations of spanwise (dashed lines) and streamwise (dotted lines) planar cuts in mm.

F. Direct Force Measurement

The influence of the DBD plasma actuator in quiescent air is typically measured by two figures of merit: the peak velocity induced and the average resultant thrust. Here we focus on the experimental setup to measure the resultant thrust (FIG. 7). The thrust produced by the plasma actuators was measured directly using an Ohaus precision balance (Adventurer™ Pro AV313C) which has a resolution of 1 mg. The actuator was mounted to the scale via an acrylic stand which protruded through a small opening in the Faraday's cage. The purpose of the cage is to shield the balance from the electromagnetic noise present due to the high electric fields required to generate the plasma discharge. Due to the scale's high sensitivity, the slightest ambient room currents were found to significantly affect the measured resultant thrust. To resolve this issue the setup was housed in a large quiescent chamber with dimensions 0.61 m x 0.61 m x 1.22 m (width x depth x height). High voltage leads were connected to the actuator with 34 AWG magnetic wires in order to prevent wire droop from influencing the reading. Additional information regarding this setup may be found in reference 18.

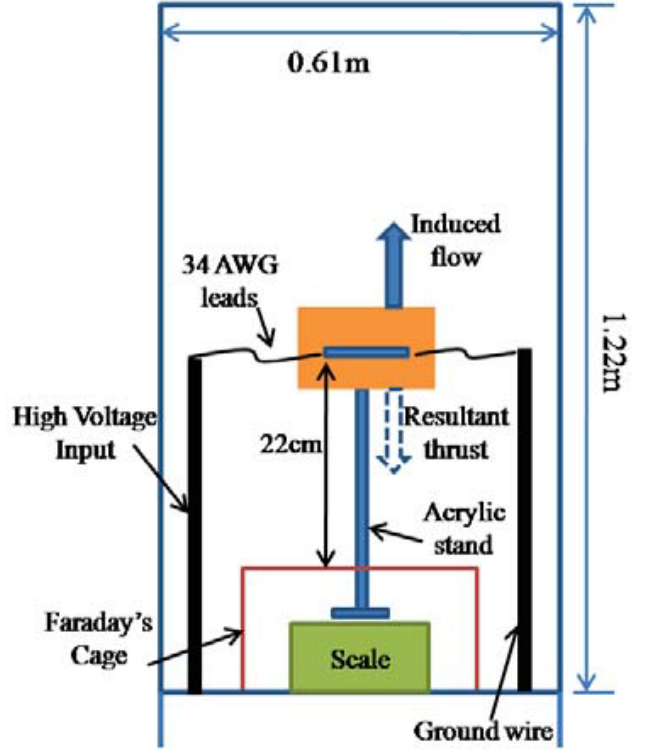


FIG. 7. Experimental setup for direct force measurements of a DBD plasma actuator.

IV. RESULTS AND DISCUSSIONS

A. Numerical Results of the Plasma Actuators

We assume a time averaged electric plasma force as a body source term in the flow domain. The intensity of the plasma force is based on the electric field and charge separation. One way to examine the variation of plasma force distribution is to measure electron temperature shown in FIG. 8. For weakly ionized gas, the electron temperature (\sim eV) can be two orders of magnitude higher than the ions or neutral species. Basically, the electron temperature is proportional to the ratio E/N (electric field/neutral density). We can see higher concentration of the electron temperature due to the geometric effects.

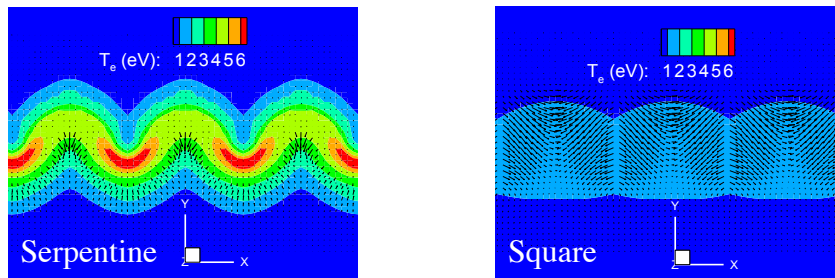


FIG. 8. Electron temperature contour on the xy-plane for serpentine and square actuators.

Figure 9 shows force vectors overlaid on potential contours in the xy -plane ($z = 0$) for serpentine and square actuators. In the figure the force vectors are acting from the powered electrode to the grounded electrode. For the both actuators, the force vectors follow the shape of powered electrode. Therefore one can say that the shape of the electrodes dominate the distribution of the electric plasma force vectors. Figure 9 also shows electric force vectors overlaid on force (F_y) contours in the yz -plane ($x = 0$) at center of the actuator. From FIG. 9, it is clear to see the force distributions are purely three-dimensional for serpentine and square designs.

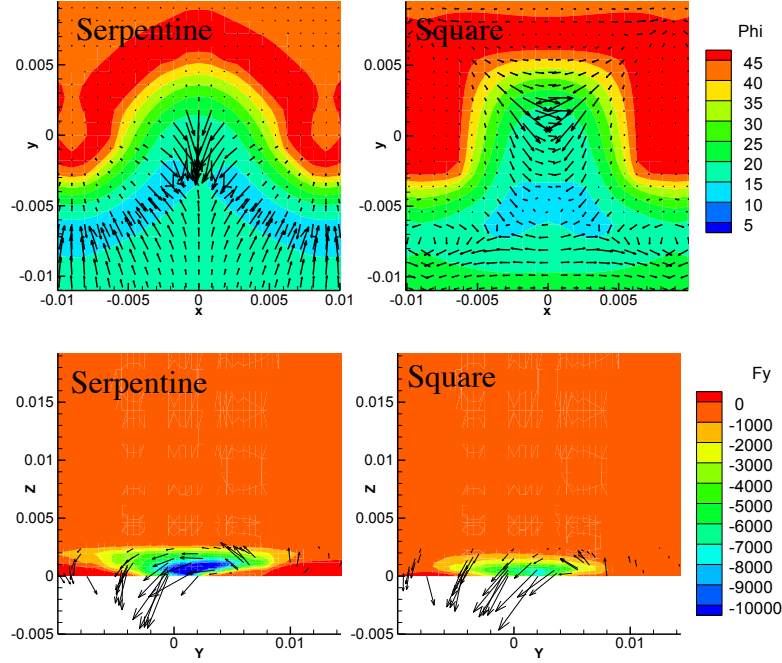


FIG. 9. Plasma force vectors overlaid on potential contour (Φ) and force contour (F_y) in y -direction at yz -plane for four different designs.

Figure 10 shows the streamtraces overlaid on vertical velocity contour (z -velocity) for the yz -plane ($x = 0$). We can see the flow is attracted from the inlet (right) and is pinched at center ($y = 0$) of the domain, and then moves forward downstream of the actuators. These arrow headed lines also show that the flow is rapidly moving downward and upward downstream after the pinching region. For the serpentine and square designs, the pinching effects result in a large normal velocity way from the wall. Here, the plasma jet issuing angle is 33 degrees for square actuators. Based on jet angles of the plasma actuators, we can say that three-dimensional square actuator has much stronger pinching effects than the two-dimensional linear actuator. Figure 10 also shows instantaneous three-dimensional vortical structures that are induced by serpentine and square actuators after 16 milliseconds of operation. In FIG. 10, the iso-surfaces colored by red and blue depict y -vorticity at ± 1000 1/sec. The y -vorticity (ω_y , i.e. streamwise vorticity) is defined as curl of fluid velocity determined by the derivative in the spanwise ($\partial u/\partial z$) and vertical ($\partial w/\partial x$) directions. For three-dimensional (serpentine and square) actuators, both $\partial u/\partial z$ and $\partial w/\partial x$ terms are important for vorticity generation. Specially, the term of $\partial u/\partial z$ dominates flow field for serpentine and square actuators. The term of $\partial u/\partial z$ can be used to represent the rapid changes in spanwise velocity which causes pinching and spreading effects. The pinching effect changes the flow direction from surface normal to surface parallel while the spreading effect pushes the fluid outward and forward downstream of the actuator. When both effects happen at same the time, they make fluid rapid rotational and translational motions in all three directions. Notably serpentine and square actuators are capable

of inducing mixing much further downstream (in y-direction) than the baseline two-dimensional linear actuator. For the square actuator, it has much bigger size of y-vorticity than other designs. So it will be very useful to induce a strong flow mixing as a vortex generating device.

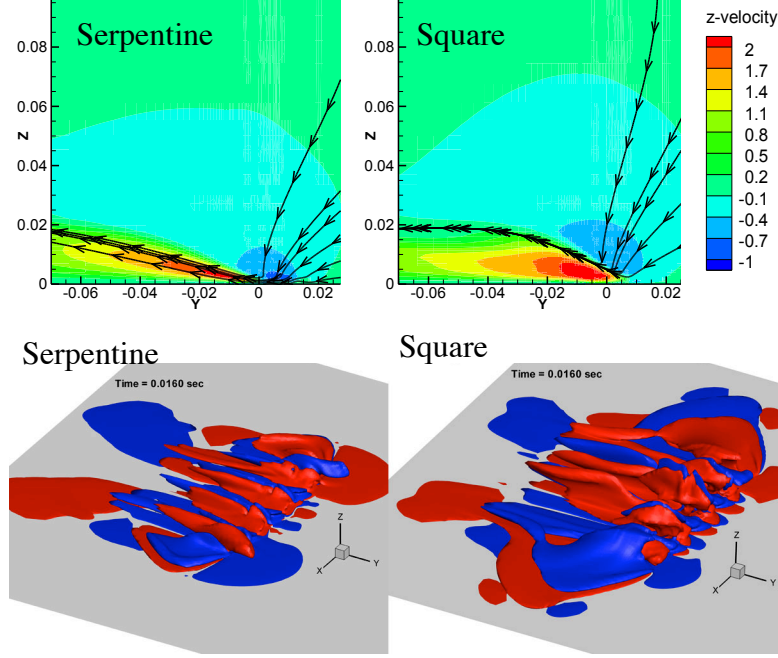


FIG. 10. Streamtraces overlaid on vertical velocity contour (z-velocity) and three-dimensional dynamics of y-vorticities (± 1000 1/s) at 16 ms.

From the previous discussion we observed that the serpentine and square actuators have a much stronger three-dimensional effect on the flow than linear actuator. In order to further explore the design space of these configurations, the wavelength (λ) and/or amplitudes (Λ) is varied. The influence of different wavelengths ($\lambda = 10, 20, 30$ mm) or amplitudes ($\Lambda = 4, 8, 16$ mm) is presented shown in FIG. 11. It is obvious to see that the vertical velocity of the flow increases as the wavelengths increases from $\lambda = 10$ to $\lambda = 20$ mm for both designs. On the contrary, for a fixed wavelength (10 mm) varying the amplitude has little effect of the resultant vertical velocity for either design. The large increase in vertical velocity for the square configuration as compared to the serpentine actuator is attributed to the larger ionized area/region produced by the square design. In particular the jet angle increases almost 100% for as the wavelength for the square actuator increases from 10 mm to 20 mm. However, the limit of the jet angle will not increase linearly with wavelengths. As the jet angle increases the vertical component of the flow velocity increases. In other word, the decreasing jet angle means the streamwise velocity becomes dominant. So increasing wavelengths or amplitudes may bring different flow physics based on the purposes of the plasma actuators for different applications.

B. Experimental Data for the Plasma Actuators

As a simple first step, the laser sheet was positioned to illuminate the spanwise plane cutting through the trough of serpentine actuator ($z = 0$ mm). A lit incense stick was placed ~ 5 mm upstream of the exposed electrode, the actuator was turned on, and the image was captured using a Nikon D90 SLR camera. The result of this rudimentary test indicates a vertically vectored momentum component along the plane. The flow is pushed away from the surface at approximately a 43° angle (FIG. 12). As a comparison, smoke flow visualization with a standard linear actuator shows that the induced jet creates a $\sim 12^\circ$ angle with the surface

(FIG. 12). The observed pinching of the fluid in the serpentine configuration is a result of colliding streams of fluid accelerated due to the plasma body force. This force acts perpendicular to the curvature of the exposed electrode driving the fluid parallel to the dielectric surface. However, since the serpentine design also consists of a neighboring spreading region at the crest of the actuator the existence of a truly three-dimensional flow field is natural.

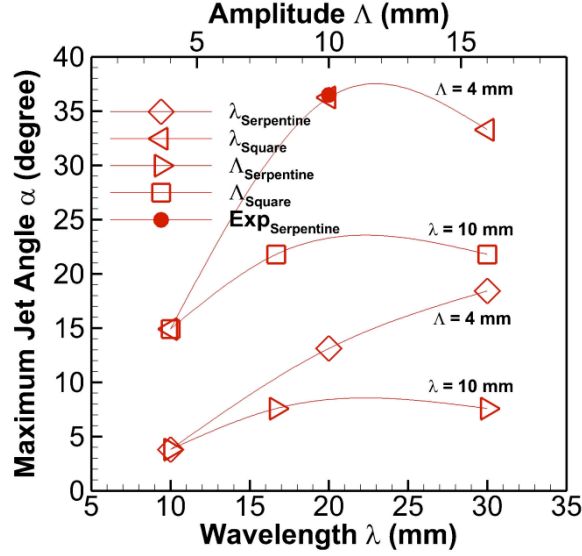


FIG. 11. Comparison of the jet angles induced by serpentine and square actuators with different wavelengths and amplitudes.

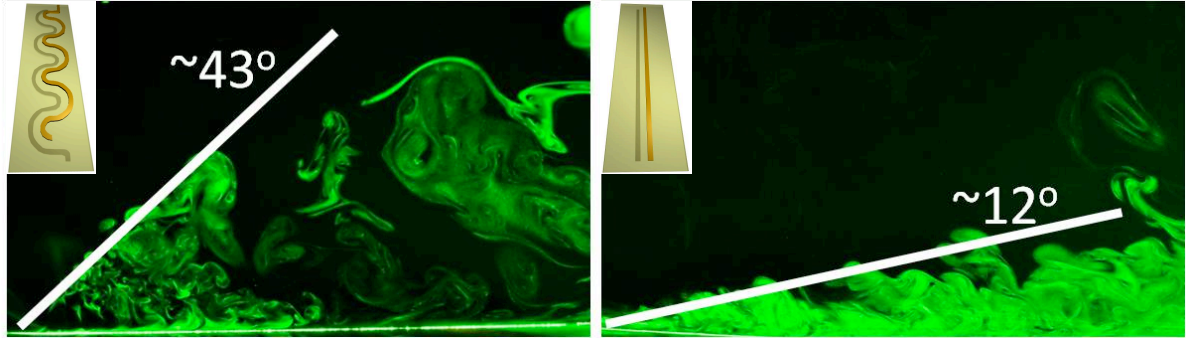


FIG. 12. Smoke flow visualization: serpentine actuator (left, plane taken along the trough, $z = 0$ mm) and standard linear actuator (right).

Select results from the streamwise scan of the circular serpentine actuator are shown in figure 13, which depicts contours of the streamwise vorticity. These results show pairs of vectored counter-rotating vortices which are centered along the $z = 0$ and -20 mm planes (the troughs of the actuator). The vortices begin to form around the inflection point ($x = 6$ mm) of the curve making up the exposed electrode and continue to grow in magnitude as they propagate downstream. The growth of the vortex pairs is clearly seen in figure 13d. These results agree well with prior numerical prediction³ of the existence of such a flow structure. However, one may also notice the lack of symmetry between the vortex pair located at $z = 0$ mm and -20 mm. The asymmetry

appears to worsen the further downstream. Such a result is most likely due to slight variations in the plasma body force along the span of the actuator, which results in a non-uniformity in the flow field.

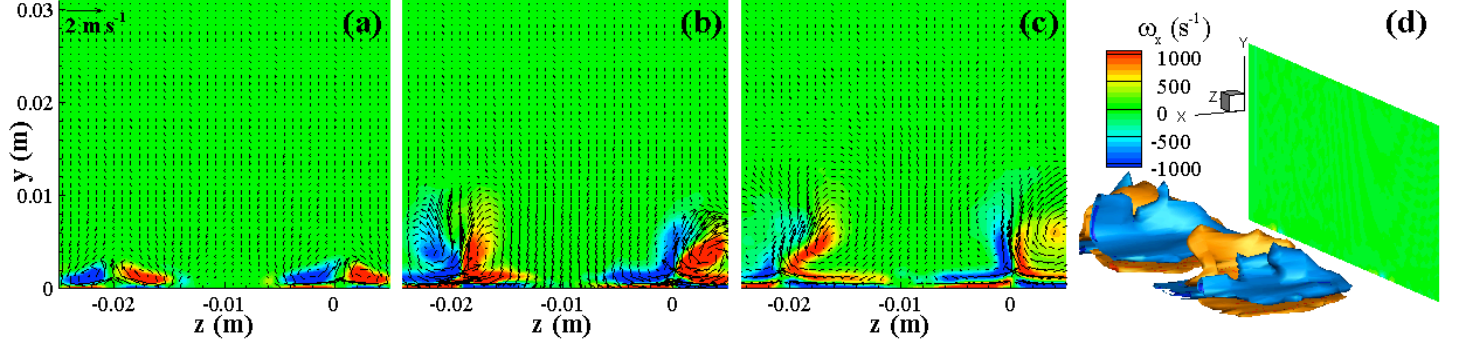


FIG. 13. Time averaged contour plots and iso-surfaces of streamwise vorticity (s^{-1}) for a serpentine actuator with an input voltage of 14 kVpp. (a) $x = 7.5$ mm, (b) $x = 12.5$ mm, (c) $x = 17.5$ mm, and (d) a three-dimensional perspective view (the green plane indicates $x = 0$ mm).

The combination of both spanwise and streamwise vorticity generation creates a unique structure in the induced flow field for the serpentine configurations. As shown by the streamtraces in figure 14, which are reconstructed from the streamwise scan, the fluid follows a corkscrew like path as it is entrained in the troughs of the actuator. The vectored pinching of the fluid in this region pushes the fluid forward and away from the surface as u_z imparts a spin on its path. The fluid at the crest of the rectangular actuator is simply pushed forward. A similar corkscrew like path was obtained from the spanwise scan, as well as for the circular serpentine design.

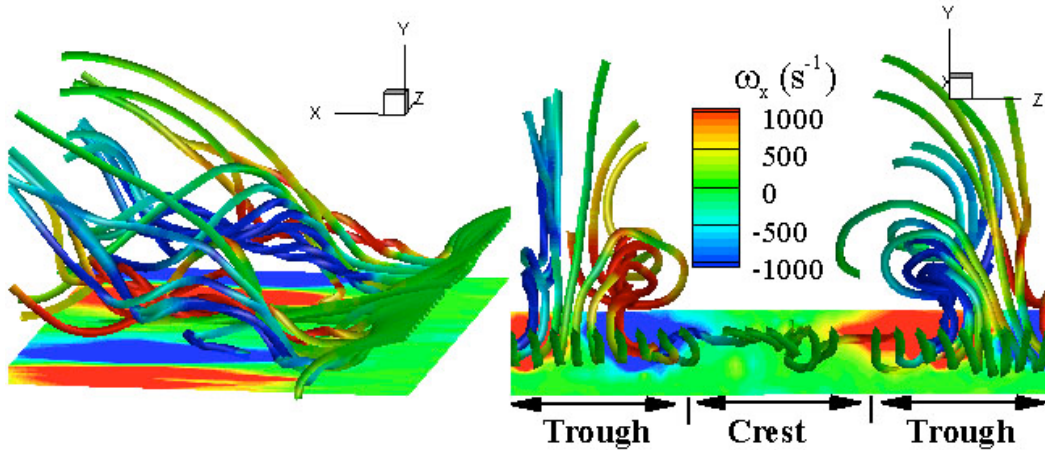


FIG. 14. Streamtraces colored by streamwise vorticity (s^{-1}) showing a corkscrew like structure in the induced flow field.

Figure 15 represents the vertical velocity contours for a square actuator that closely validates the numerical prediction with experimental data. The relative agreement between the numerical and experimental findings provides some confidence that the numerical model is capable of predicting reasonable flow characteristics resulting from DBD actuation.

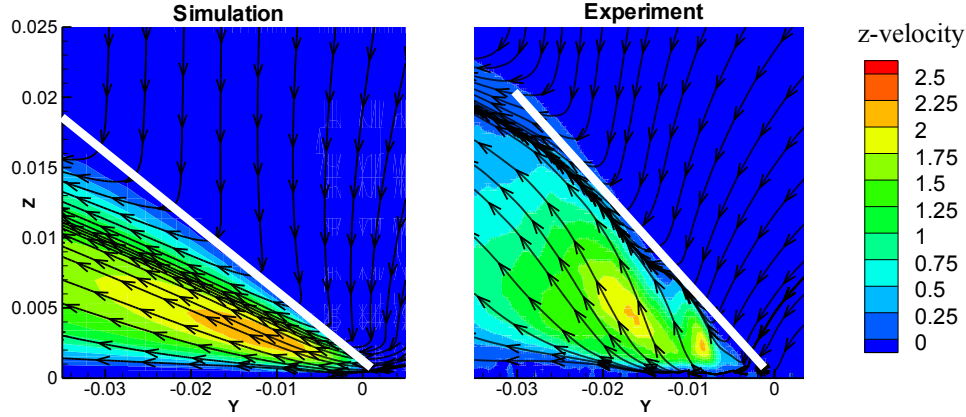


FIG. 15. Vertical velocity contour validation with experimental data for a square actuator.

The average calculated power consumption for each device is presented in table 1. When normalized by the spanwise length, l_{span} , the linear actuator clearly used the least amount of power, while the square design consumed the most. However considering the total length of the electrode, l_{tot} , that accounts for the winding electrode, the normalized power variations between the designs drastically reduces. This result indicates that the ionization process may not be affected by the geometric manipulation of the electrodes. In the serpentine design one is only affecting the direction in which the plasma body force is oriented. However, from a design perspective, the ultimate goal is to apply these actuators to real world aerodynamic flows such as over an airfoil. In such a case the actuator would most likely be applied over some unit length of the airfoil, where P_{tot}/l_{span} would be the more appropriate design parameter.

Table 1. Average power consumption for geometries tested (14kVpp input)

	P_{tot} (W)	P_{tot}/l_{span} ($W m^{-1}$)	P_{tot}/l_{tot} ($W m^{-1}$)
<i>Linear actuator</i>	2.6 ± 0.5	16.3 ± 3.1	16.3 ± 3.1
<i>Serpentine actuator</i>	4.8 ± 0.6	30.0 ± 3.7	19.1 ± 2.4
<i>Square actuator</i>	7.2 ± 0.8	40.0 ± 4.4	20.0 ± 2.2

C. Experimental Data for the Multi-barrier Actuators

A comparison between a standard actuator, a bi-layer MBPA, and a tri-layer MBPA is shown in figure 16 for both resultant thrust and effectiveness. One can see from the figure that for a constant total voltage and a constant overall thickness of the dielectric, that the standard actuator produces more thrust than the MBPA configurations. These results are consistent with prior preliminary data.¹⁸ Conversely, when one compares the designs on an effectiveness basis (FIG. 16b) the bi-layer MBPA clearly outperforms the other designs. An increase in effectiveness of $\sim 160\%$ is shown for a bi-layer configuration over the standard actuator. This fact has significant system level design implications. Although not producing a higher force the bi-layer MBPA provides more force for a given amount of power. This allows one to reduce the size and weight of the required power supply. The design also allows the high voltage to be distributed between multiple electrodes. This then reduces the voltage requirements of an individual power supply; for instead of requiring a 30 kV source one can

simply use two 15 kV power supplies. Logic then follows that a decrease in output voltage further reduces the size and weight of the power supply.

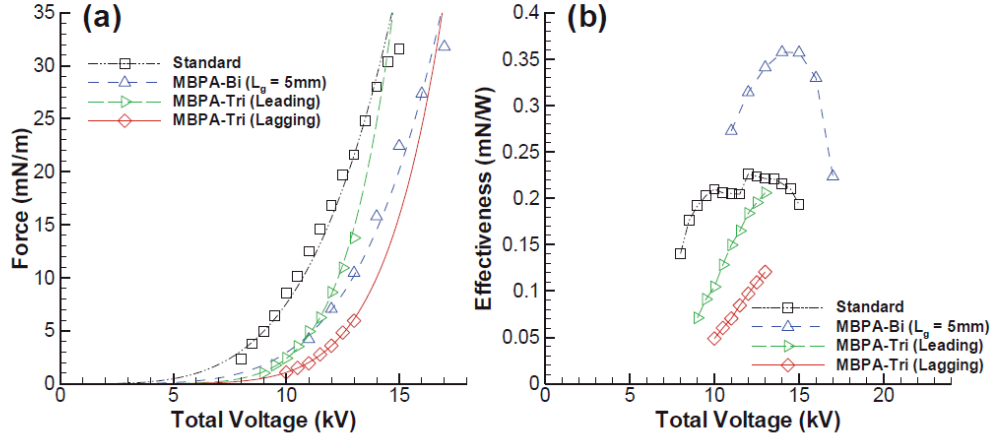


FIG. 16. Comparison of actuator configurations: a) force and b) effectiveness.

Questions remain through, what makes the bi-layer more effective than the standard and why the tri-layer design is the least effective? To address the former it was shown above that the total power supplied to a bi-layer MBPA when the middle grounded electrode is present, particularly at low voltages, is primarily consumed by the exposed electrode. As such the current flowing through that branch in the circuit should account for approximately 100% of the total current delivered to the device. Therefore, one may ignore the encapsulated electrode in the bi-layer MBPA and simply compare the instantaneous current waveform of the exposed electrode with that of the standard design (FIG 17). When looking at the comparison found in figure 17 one observation stands out in particular. That is, the peak current reached is higher for the standard actuator. Based on this remark it is reasonable to postulate that since Joule heating is proportional to I^2 that the standard actuator is physically heating up more than that of the MBPA, with the waste heat contributing little to the momentum coupling of the surrounding fluid. Although no temperature measurements have been made to date, future tests will be conducted using an IR camera to verify this experimentally.

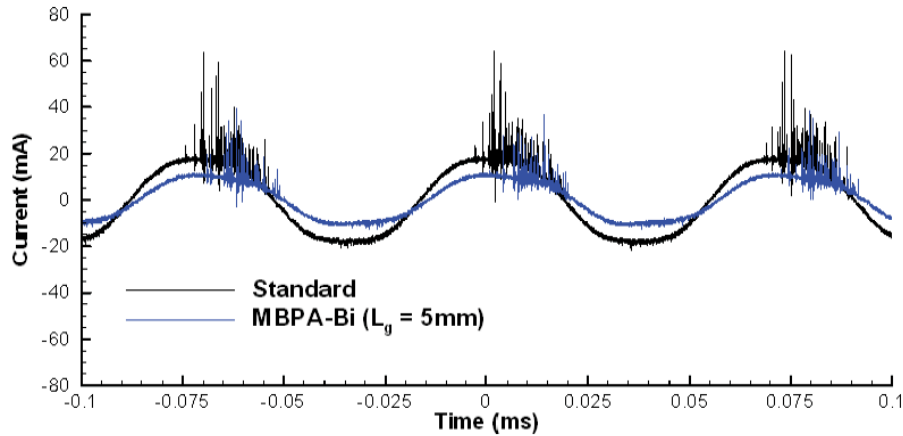


FIG. 17. Instantaneous current waveforms for a standard actuator and bi-layer MBPA (exposed/top electrode only) for a total voltage of 13kV.

The second question proposed above about the ineffectiveness of the tri-layer design is a harder one to answer. The simple response would be that this particular geometry chosen was not optimal. For the tri-layer design the total separation length between the exposed and encapsulated electrode was 10 mm (or $2w$ figure 4c). Whether or not such a large separation is the root cause in the poor performance of the tri-layer still needs to be explored and future MBPA designs will address this question by decreasing the width of sandwiched electrodes.

V. CONCLUSIONS

The plasma governing equations as well as Navier-Stokes equations were solved with our in-house MIG flow code and commercial software. The configurations of serpentine and multi-barrier actuators are introduced in the present study. It was numerically predicted that the serpentine designs are capable of producing significant three-dimensional effects which leads to enhanced mixing of the surrounding fluid. Electron temperature distribution is also shown based on the concentration of electric field. The effect of wavelength (λ) and/or amplitudes (Λ) of the actuators was also investigated. It was found that the induced vertical velocity in the vicinity of the plasma region is proportional to the actuators wavelengths. A maximum jet angle at the trough of the actuator was numerically predicted to be $\sim 36^\circ$. Experimental data helps validate this predication with a measured jet angle of $\sim 35^\circ$ for a serpentine actuator. Also, stereo-PIV has been used to capture the complicated three-dimensional flow field induced by serpentine plasma actuators in a quiescent environment. We note that the serpentine configuration combines the effects of a linear plasma synthetic jet actuator and that of a linear DBD actuator, both of which are inherently quasi two-dimensional. As a result there is a vectored nature to the vortex generation in the serpentine design. This was shown to result in a corkscrew like structure in the induced flow field.

In order to increase the effectiveness of plasma actuators, an exploration of the MBPA design space has been carried out. The influence that the middle electrodes width has on the performance of a bi-layer MBPA has been ascertained. The middle electrode was found to play an important role in how the consumed power was disturbed amongst the powered electrodes. When power consumption was taken into account, the bi-layer configuration significantly outperformed the other designs. An improvement in effectiveness of $\sim 160\%$ is shown for a bi-layer configuration over the standard actuator.

We believe that both serpentine and multi-barrier plasma actuators have numerous aerodynamic applications where an increased mixing of the local fluid is desired. The areas of boundary layer transition, convective heat transfer, and plasma assisted combustion (PAC)²³ all contain flow fields in which an improvement in flow turbulization could significantly enhance the desired output. An experimental study using a serpentine actuator on a freestream boundary layer of such an application remains open for evaluation in the near future. We expect the geometric design of the serpentine device would be strongly dependent on the boundary layer characteristics of any given application. The influence on flow structure and controllable vectoring of a segmented serpentine design and the addition of a duty cycle to the supply voltage will be evaluated in future efforts.

ACKNOWLEDGMENTS

This work was sponsored in part under Air Force Office of Scientific Research Grants #FA9550-09-1-0615 and #FA9550-09-1-0372 monitored by Drs. Doug Smith and Charles Suchomel.

REFERENCES

- ¹E. Moreau, "Airflow control by non-thermal plasma actuators," J. Phys. D: Appl. Phys. 40, 605 (2007).
- ²T. C. Corke, C. L. Enloe and S. P. Wilkinson, "Dielectric barrier discharge plasma actuators for flow control," Annu. Rev. Fluid Mech. 42, 505 (2010).

- ³S. Roy and C.-C. Wang, "Bulk flow modification with horseshoe and serpentine plasma actuators," J. Phys. D: Appl. Phys. 42, 032004 (2009).
- ⁴A. Santhanakrishnan and J. Jacob, "Flow control with plasma synthetic jet actuators," J. Phys. D: Appl. Phys. 40 (3), 637-651 (2007).
- ⁵D. P. Rizzetta and M. R. Visbal, "Effect of plasma-based control on low-Reynolds number flapping airfoil performance," 49th AIAA Aerospace Sciences Meeting, AIAA 2011-735.
- ⁶D. P. Rizzetta, and M. R. Visbal, "Numerical investigation of plasma-based control for low-Reynolds-number airfoil flows," AIAA Journal 49 (2), 411-425 (2011).
- ⁷J. R. Roth, D. M. Sherman and S. P. Wilkinson, "Boundary layer flow control with a one atmosphere uniform glow discharge surface plasma," 36th AIAA Aerospace Sciences Meeting and Exhibit (Reno, NV, 1998), AIAA-98-0328.
- ⁸T. C. Corke, E. J. Jumper, M. L. Post, D. M. Orlov and T.E. McLaughlin, "Application of weakly-ionized plasmas as wing flow-control devices," 40th AIAA Aerospace Sciences Meeting and Exhibit (Reno, NV, 2002), AIAA-2002-350.
(2005).
- ⁹W. Shyy, B. Jayaraman and A. Andersson, "Modeling of glow discharge-induced fluid dynamics," J. Appl. Phys. 92, 6434 (2002).
- ¹⁰D. M. Orlov and T.C. Corke, 43rd AIAA Aerospace Sciences Meeting and Exhibit (Reno, NV, 2005), AIAA-2005-1083.
- ¹¹K. P. Singh and S. Roy, "Force approximation for a plasma actuator operating in atmospheric air," J. Appl. Phys. 103, 013305 (2008).
- ¹²K. P. Singh and S. Roy, "Modeling plasma actuators with air chemistry for effective flow control," J. Appl. Phys. 101, 123308 (2007).
- ¹³S. Roy, "Flow actuation using radio frequency in partially ionized collisional plasmas," Appl. Phys. Lett. 86, 101502 (2005).
- ¹⁴H. Kumar and S. Roy, "Multidimensional hydrodynamic plasma-wall model for collisional plasma discharges with and without magnetic-field effects," Phys. Plasmas 12, 093508 (2005).
- ¹⁵K. P. Singh, S. Roy and D.V. Gaintonde, "Modeling of Dielectric Barrier Discharge Plasma Actuator with Atmospheric Air Chemistry," 36th AIAA Fluid Dynamics and Flow Control Conference (San Francisco, CA, 2006), AIAA-2006-3381.
- ¹⁶D. M. Schatzman and F. O. Thomas, "Turbulent boundary layer separation control with plasma actuators," 4th Flow Control Conference. AIAA 2008-4199.
- ¹⁷S. Roy, "Method and Apparatus for Multibarrier Plasma Actuated High Performance Flow Control," Patent WO 2009/005895, Published Jan 8, 2009 (filed May 2007).
- ¹⁸R. Durscher and S. Roy, "Novel Multi-Barrier Plasma Actuators for Increased Thrust," 48th AIAA Aerospace Sciences Meeting Including the New Horizons Forum and Aerospace Exposition (Orlando, FL, 2010), AIAA Paper 2010-965.
- ¹⁹C.-C. Wang and S. Roy, "Three-dimensional simulation of a micro plasma pump," J. Phys. D: Appl. Phys. 42, 185206 (2009).
- ²⁰G. A. Galechyan, "Controlling the electron temperature in plasma," Laser Physics 5, 731 (1995).
- ²¹TSI 2000 Model 9302 Atomizer, Instruction Manual.
- ²²DaVis 7.2, Instruction Manual, LaVision GmbH, December, 2007
- ²³C.-C. Wang and S. Roy, "Combustion stabilization using serpentine plasma actuators," Appl. Phys. Lett. 99, 041502 (2011).